


Ultra-low voltage resistive switching of HfO_2 buffered (001) epitaxial NiO films deposited on metal seed layers

Cite as: Appl. Phys. Lett. **111**, 142103 (2017); <https://doi.org/10.1063/1.4990089>

Submitted: 14 June 2017 . Accepted: 24 September 2017 . Published Online: 04 October 2017

X. Y. Qiu , R. X. Wang, Z. Zhang, M. L. Wei, H. Ji, Y. Chai, F. C. Zhou, J. Y. Dai, T. Zhang, L. T. Li, and X. S. Meng



View Online



Export Citation



CrossMark

ARTICLES YOU MAY BE INTERESTED IN

[Enlarged read window in the asymmetric ITO/ \$\text{HfO}_x\$ /TiN complementary resistive switch](#)

Applied Physics Letters **111**, 043501 (2017); <https://doi.org/10.1063/1.4995252>

[Combination of conductive filaments and Schottky behavior in multifunctional \$\text{Sn}_{1-x}\text{Cu}_x\text{O}_{2-\delta}\$ memristor](#)

Applied Physics Letters **111**, 143503 (2017); <https://doi.org/10.1063/1.5005803>

[Molybdenum oxide-base phase change resistive switching material](#)

Applied Physics Letters **111**, 163105 (2017); <https://doi.org/10.1063/1.5000410>

Lock-in Amplifiers
Find out more today



Zurich
Instruments

AIP
Publishing

Ultra-low voltage resistive switching of HfO₂ buffered (001) epitaxial NiO films deposited on metal seed layers

X. Y. Qiu,^{1,a)} R. X. Wang,¹ Z. Zhang,² M. L. Wei,¹ H. Ji,³ Y. Chai,² F. C. Zhou,² J. Y. Dai,² T. Zhang,¹ L. T. Li,¹ and X. S. Meng¹

¹School of Physical Science and Technology, Southwest University, Chongqing 400715, China

²Department of Applied Physics, The Hong Kong Polytechnic University, Hong Kong, China

³School of Energy Science and Engineering, University of Electronic Science and Technology of China, Chengdu 610054, Sichuan, China

(Received 14 June 2017; accepted 24 September 2017; published online 4 October 2017)

A set of (001) epitaxial NiO films were prepared on highly textured (001) Pt seed layers using magnetron sputtering, and their resistive switching performance was measured. Cube-to-cube epitaxial relationships of NiO(001)//Pt(001) and NiO[001]//Pt[001] were demonstrated. Current-voltage measurements revealed that the Ag/(001)NiO/(001)Pt capacitor structures exhibited stable bipolar switching behavior with an ON/OFF ratio of 20 and an endurance of over 5×10^3 cycles. Furthermore, inserting a HfO₂ buffer layer between the NiO film and the Ag top electrode increased the ON/OFF ratio to more than 10^3 and reduced the SET/RESET voltage to below ± 0.2 V. These enhancements are attributed to the differing filament growth mechanisms that occur in the NiO and HfO₂ layers. The present work suggests that Ag/HfO₂/(001)NiO/(001)Pt capacitor structures are a promising technology for next-generation, ultra-low voltage resistive switching memory. *Published by AIP Publishing.* <https://doi.org/10.1063/1.4990089>

Resistive switching random access memory (ReRAM) based on oxide films has received attention for its potential use in next-generation nonvolatile memory, logic devices, and neuromorphic computers due to its good scalability,¹ 3D stacking potential,² and operating characteristics that bear a close resemblance to those of synapses.³ These applications require ReRAM cells to exhibit low ON/OFF-state currents but high ON/OFF ratios. The binary metal oxide NiO has been investigated extensively as a ReRAM candidate since the 1960s.⁴ Nevertheless, the structural inhomogeneity of polycrystalline NiO films often leads to varying resistive switching behaviors including unipolar, bipolar, or threshold-type resistive switching, largely depending on the details of the fabrication technologies used.^{5–10} Epitaxial NiO films can be expected to exhibit much more consistent resistive switching than polycrystalline/amorphous NiO films due to their good structural homogeneities and low defect densities. Resistive switching of single-crystalline NiO structures such as nanowires and ultra-thin epitaxial films has been addressed. Epitaxial NiO thin films have been deposited on various oxide substrates or seed layers such as MgO,¹¹ Nb-doped SrTiO₃,^{12,13} SrRuO₃,¹⁴ and Pt_{0.8}Ir_{0.2}.¹⁵ It is noted that the metal seed layers might serve as both effective substrates for epitaxial growth of NiO films and good bottom electrodes, as resistive switching memory devices usually have metal-insulator-metal capacitor structures.

Nevertheless, epitaxial growth of NiO films on metal seed layers has been rarely reported thus far. In this work, we use highly textured (001) Pt films as metal seed layers, noting that a large positive lattice mismatch between NiO (lattice constant: 4.18 Å) and Pt (lattice constant: 3.92 Å) exists. However, NiO has a thermal expansion coefficient of

$7.8 \times 10^{-6} \text{ K}^{-1}$ at 300 K,¹⁶ which is smaller than that of Pt ($8.8 \times 10^{-6} \text{ K}^{-1}$ at 300 K).¹⁷ The negative thermal mismatch between NiO and Pt creates an opportunity to achieve the epitaxial growth of (001) NiO films on (001) Pt layers at sufficiently high deposition temperatures. Fortunately, the referenced stacking system exhibits excellent, stable bipolar resistive switching properties.

In our experiments, Pt plates (99.99% purity), Ni plates (99.99% purity), and dense HfO₂ ceramic disks (99.99% purity) were used as sputtering targets. (001) MgO single-crystal substrates were pre-treated using the method described in our previous work.¹⁸ Deposition details and property characterizations of the 50 nm-thick (001) Pt seed layer, 100 nm-thick NiO film, and 30 nm-thick HfO₂ layer are presented in the [supplementary material](#). The crystallinities of the as-prepared NiO films on Pt seed layers were checked via X-ray diffraction (XRD), and the resulting $\theta/2\theta$ spectra are presented in Fig. 1 with intensity on a logarithmic scale. The spectra include those from the bare Pt seed layer

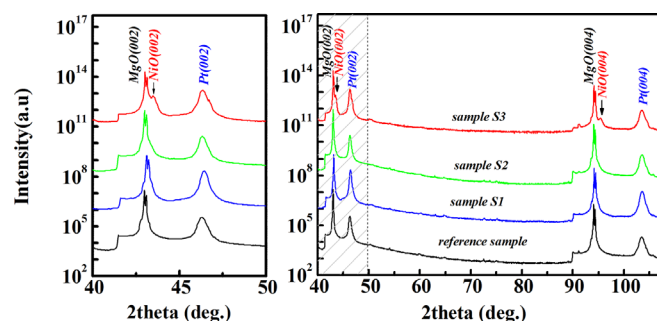


FIG. 1. Theta/2theta XRD patterns for the reference sample, sample S1, sample S2, and sample S3. The left small figure shows the magnified XRD pattern within the range of 40°–50° (corresponding to the dashed line area in the right figure).

^{a)} Author to whom correspondence should be addressed: qxy2001@swu.edu.cn

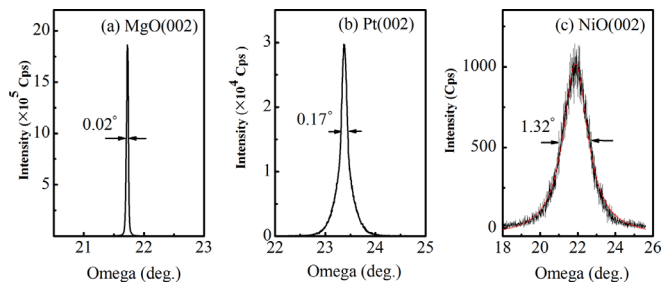


FIG. 2. Rocking curves of the (002) reflections from (a) the MgO substrate, (b) Pt seed layer, and (c) NiO film for sample S3.

on a (001) MgO substrate (reference sample) and three NiO films deposited at 280 °C with no post-annealing (sample S1), post-annealing at 480 °C for 30 min (sample S2), and post-annealing at 680 °C for 30 min (sample S3). The {001} peaks from MgO and the Pt seed layer are visible in all samples, but the {001} peaks from NiO can be seen only in sample S3. This suggests that the NiO films in samples S1 and S2 are amorphous. In sample S3, the (001) NiO reflections overlap heavily with those from (001) MgO due to their almost identical (001) lattice spacing.

The absence of NiO peaks other than the {001} reflection from sample S3 suggests possible epitaxy of NiO on the {001} Pt seed layer. Figure 2 shows the rocking curves and corresponding full width at half maximum (FWHM) results from the (002) reflections from the MgO substrate, Pt seed layer, and NiO film in sample S3. The Pt seed layer shows a large amount of (001)-texture with a FWHM of only 0.17°, while the NiO film exhibits less texture because the FWHM value is 1.32°. ω -2 θ high resolution XRD patterns and X-ray reflectivity spectra [Figs. S1(a) and S1(b), [supplementary material](#)] for sample S3 and a reference sample indicate apparent “oscillation” peaks around the Pt (002) peak. A relatively detailed discussion on “oscillation” peaks is given in the [supplementary material](#).

We checked the in-plane mosaicity of sample S3 using ϕ -scan data on the {111} reflections of NiO, Pt, and MgO. The NiO (111) reflection shows the strongest diffraction intensity second to the (001) plane, according to standard ICDD data (PDF #47-1049). As shown in Fig. 3, all the three sets of ϕ -scan spectra exhibit 4-fold symmetry, thus

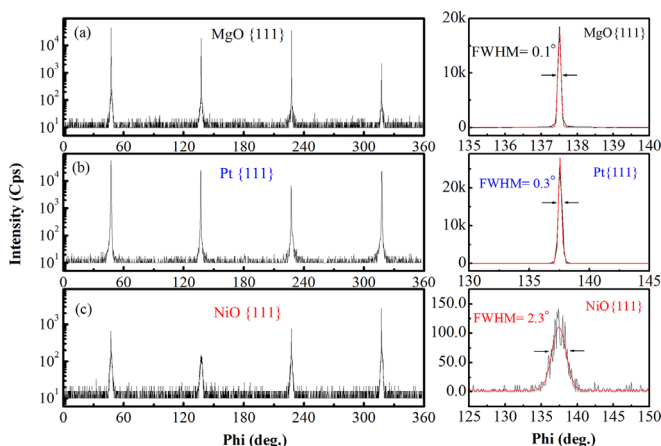


FIG. 3. X-ray ϕ -scan patterns and FWHM of (a) MgO{111}, (b) Pt{111}, and (c) NiO{111} diffraction for sample S3.

demonstrating the good in-plane epitaxial relationship between the NiO film, Pt seed layer, and MgO substrate. However, the in-plane mosaicity of the NiO film is worse than that of the Pt seed layer due to the large (111) FWHM of 2.3°. The FWHMs of the Pt layer and MgO substrate are 0.3° and 0.1°, respectively. On the other hand, there are intensity differences between the four diffraction peaks in the ϕ -scans of both Pt {111} and NiO {111}. This is because there is always some tilting or dilation (strain) in both the Pt layer and the NiO film due to the lattice and thermal mismatches at the Pt/MgO and NiO/Pt interfaces.

The as-prepared films were also checked via transmission electron microscopy (TEM), focusing on the interfaces between layers. The cross-sectional TEM image in Fig. 4(a) shows the rough surface and columnar microstructure of the NiO layer, while the NiO-Pt and Pt-MgO interfaces are clear. As shown in Fig. 4(b), the atomically sharp NiO-Pt interface and the absence of Moiré fringes and grain boundaries evidence the excellent epitaxial growth of the NiO film on the Pt seed layer. The selected-area diffraction patterns (SADPs) shown in Fig. 4(c) map (001) NiO and (001) Pt diffraction dots that comply with 4-fold symmetry, suggesting “cube-on-cube” growth of the NiO film on the Pt seed layer. The Pt-MgO interface shown in Fig. 4(d) is free of voids, distortions, and dislocations. The corresponding SADPs [Fig. 4(e)] illustrate two nested sets of 4-fold symmetric diffraction dots from {001} Pt and {001} MgO and the presence of “cube-on-cube” epitaxial growth of the Pt layer on a MgO substrate.

It is interesting to find that the NiO film in sample S3 exhibits a percolating network-like morphology infiltrated with interconnected nanopores although it does grow epitaxially on the Pt seed layer, as shown via the scanning electron microscopy (SEM) image in Fig. 5(a). These nanopores may result from the surface reconstruction of the NiO film during post-annealing that may be driven by thermal and lattice mismatch stresses. The stoichiometry of the film matches that of NiO, as evidenced by the X-ray photoelectron spectroscopy (XPS) spectrum of the Ni 2p core level shown in the inset. The binding energy of the Ni 2p core level is consistent with that of NiO, revealing the stoichiometry. Nevertheless, depositing a 30 nm-thick amorphous HfO₂

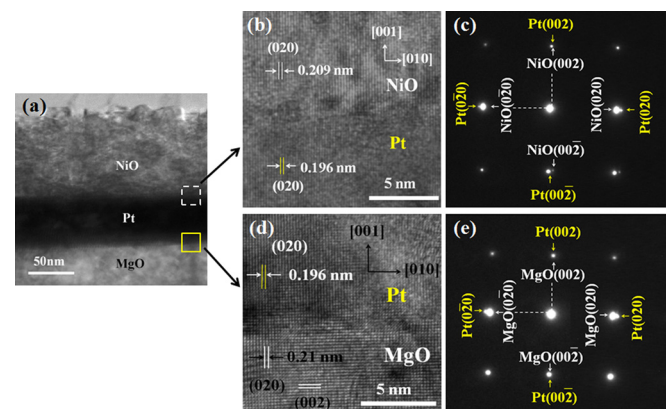


FIG. 4. (a) Cross-sectional TEM image of sample S3; (b) TEM image of the NiO/Pt interface inside the dashed white box region in Fig. 4(a); and (c) corresponding SADP. (d) TEM image of the Pt/MgO interface inside the solid yellow box region in Fig. 4(a); and (e) corresponding SADP.

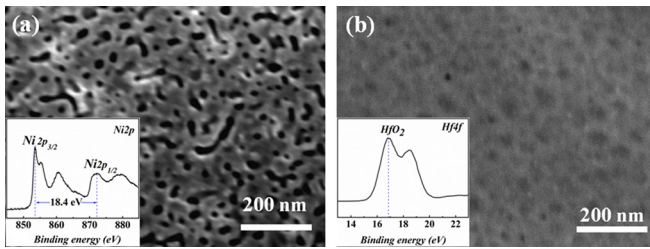


FIG. 5. SEM images of sample S1 (a) before and (b) after covering with a 30 nm-thick HfO_2 layer. Insets are XPS spectra of the Ni2p and Hf4f core-level, respectively.

buffer layer on the NiO film surface improves the surface morphology remarkably, resulting in a flat, dense, pore-free surface shown in Fig. 5(b). The binding energy of the Hf 4f core-level (17 eV) suggests that the HfO_2 buffer layer is stoichiometric as well. Certainly, covering the NiO film with such an amorphous HfO_2 buffer would be expected to improve the electrical properties of the whole structure when evaluated as a memristor cell.

In this section, we focus on the electrical and memristor behavior properties of the as-prepared samples. We discuss two memristor cells: one is the Ag/NiO(001)/Pt capacitor structure (Cell C1) and the other is the HfO_2 -buffered Ag/ HfO_2 /NiO(001)/Pt capacitor structure (Cell C2), where the NiO films were deposited at 280 °C and post-annealed at 680 °C for 30 min (similar to sample S3).

For Cell C1, the current-voltage (I-V) curves shown in Fig. 6(a) indicate stable but asymmetric bipolar switching behavior at a SET/RESET voltage lower than ± 1.0 V, without an electroforming process. This asymmetry is common if the memory cell structure includes asymmetric top and bottom electrodes, especially since Ag, Cu, W, and Al are active metals and Pt is an inert metal.^{19–21} Due to the “cone”-like metal filaments between the NiO film and the Ag layer, the tip electric field effect²⁰ is believed to be responsible for this asymmetry. Since the resistive switching behavior of Cell C1 is more apparent in the negative bias region than in the positive bias region, the endurance performance of Cell C1 is characterized only in the negative bias region. After 150 consecutive cycles, the largest OFF current is larger than 10^{-3} A, while the ON/OFF ratio is 20 at a reading voltage (V_r) of -0.4 V. The large OFF current implies relatively poor insulation of the NiO film, probably due to the surface roughness and columnar grain boundaries acting as “fast channels” for carrier flows.

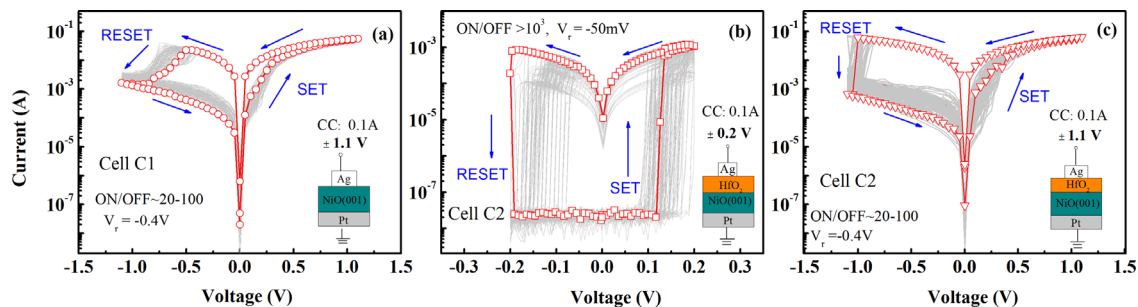


FIG. 6. Sample S3-based memory cell shows stable bipolar switching characteristics: (a) 150 consecutive cycles for cell C1 applied on ± 1.1 V sweep voltage; (b) 150 consecutive cycles for cell C2 applied on ± 0.2 V; and (c) ± 1.1 V sweep voltage. Insets in Figs. 6(a)–6(c) are the corresponding structure and measurement schematic diagrams, respectively. The Ag dot electrode area is 3.14×10^{-4} cm², and the compliance current is 0.1 A.

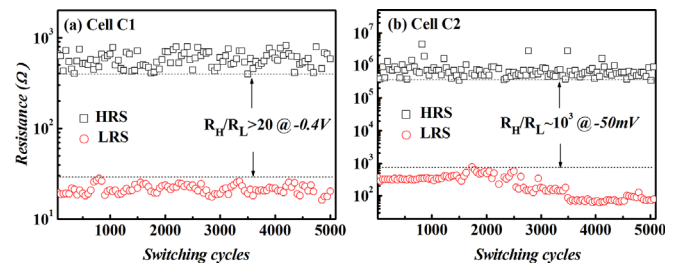


FIG. 7. Endurance property of (a) Cell C1 applied on ± 1.1 V sweep voltage and (b) Cell C2 applied on ± 0.2 V sweep voltage. Endurance measurement is employed using the DC cyclic voltammetry method with the “stair” scanning model.

However, Cell C2 with its amorphous HfO_2 buffer exhibits symmetric I-V curves [Fig. 6(b)]. The SET/RESET voltage is reduced to ± 0.2 V. The largest ON and OFF currents are reduced to 10^{-3} A and 10^{-7} A, respectively. Consequently, the ON/OFF ratio is as large as $>10^3$ even at a V_r of only -50 mV. This performance is stable after 150 consecutive ON/OFF cycles. The turn-ON/OFF slope (dV/dI) is less than 5.0 mV/dec and approaches the sharpest value (~ 1.0 mV/dec) reported thus far.^{22,23} It is believed that the amorphous HfO_2 buffer not only improves the smoothness of the NiO surface but also enhances the resistance of the cell in the OFF state. However, Cell C2 exhibits asymmetric bipolar resistive switching similar to Cell C1 when the sweep voltage is increased to ± 1.1 V. As shown in Fig. 6(c), the ON/OFF ratio decreases to between 20 and 100 in the negative bias region.

The ON/OFF switching endurance of the two samples is demonstrated in Fig. 7 by plotting the high/low resistance states (HRS/LRS) as functions of switching cycles. As shown in Fig. 7(a), the ON/OFF ratio for Cell C1 remains larger than 20 at a V_r of -0.4 V after 5×10^3 consecutive cycles at a sweep voltage of ± 1.1 V. For Cell C2, the ON/OFF ratio remains larger than 10^3 at a V_r of -50 mV after 5×10^3 consecutive switching cycles at a sweep voltage of ± 0.2 V, as shown in Fig. 7(b). This ratio decreases to ~ 20 after 400 cycles at a sweep voltage of ± 1.1 V (not shown here). The beneficial effect of the HfO_2 buffer in enhancing the ON/OFF ratio and reducing the SET/RESET voltage to ± 0.2 V is clearly demonstrated.

Furthermore, the ON/OFF switching speeds were measured and the results for Cell C2 are given in Fig. 8(a). The fastest switch from the HRS to a LRS driven by a bias pulse of 0.2 V can be completed within 250 ns, and the period for

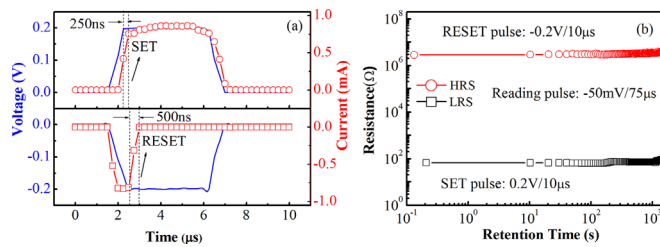


FIG. 8. Switching speed and retention performance of Cell C2: (a) it turns from HRS to LRS within 250 ns driven by a bias pulse of 0.2 V and backs to HRS within 500 ns driven by a bias pulse of -0.2 V; (b) retention performance of HRS and LRS is over 10^3 s. Voltage waveform employed for ON/OFF switch consists of ± 0.2 V SET/RESET pulses $10 \mu\text{s}$ in duration followed by -50 mV reading pulses $75 \mu\text{s}$ in duration, respectively.

back-switching to the HRS using a bias pulse of -0.2 V is 500 ns. Finally, the retention performance was characterized and the data for Cell C2 were collected by applying a voltage waveform consisting of ± 0.2 V SET/RESET pulses $10 \mu\text{s}$ in duration. The ON/OFF states were read using -50 mV pulses $75 \mu\text{s}$ in duration. The good endurance/retention performance of Cell C2 has been demonstrated, and Fig. 8(b) shows HRS and LRS retention times of over 10^3 s.

In this section, we discuss possible mechanisms of resistive switching in our C1 and C2 cells. The core question is why a thin HfO_2 buffer provides a remarkable reduction in the SET/RESET voltage. If this layer were simply a serial insulator, the SET/RESET voltage would be large. A comparison of the two cells shows that the turn-ON/OFF slope is flat for Cell C1 but is sharp for Cell C2, even though the sweep voltage is as low as ± 0.2 V. On the other hand, the OFF-state current for Cell C1 is of the same order of magnitude as the ON-state current for Cell C2. These features suggest different resistive switching mechanisms in the two cells.

In Cell C1, the NiO layer exhibits a columnar grain structure with nanopores on its surface. These nanopores are shallow and do not penetrate across the layer. Thus, they are preferential sites for current flows. On the other hand, Ag is an active metal with high ion mobility, and the migration of Ag clusters in dielectric oxide films has repeatedly been experimentally confirmed.^{24–26} In contrast, Pt is an inert metal, and the migration of Pt clusters in oxide films is reported to require a high temperature ($>900^\circ\text{C}$) and a large electric field of $3\text{--}5$ MV/cm.²⁴ However, the highest deposition/annealing temperature in our experiment is only 700°C , and the electric field employed for electrical measurements is only about 0.1 MV/cm. Thus, it is easier for Ag ions than Pt atoms to diffuse into the NiO film. Given these facts, a positive voltage easily drives Ag ions to diffuse from the top electrode into the NiO layer preferentially via the bottoms of the nanopores. This process favors the formation of cone-shaped Ag filaments across the NiO layer, as shown schematically in Fig. 9(a). Subsequent rupture of the Ag filaments may occur when a negative voltage is applied, as in an ON/OFF switching cycle.

The microscopic process of resistive switching in Cell C2 is different from the process described above and is diagrammed in Fig. 9(b). The amorphous HfO_2 layer acts as a barrier to the formation of Ag filaments across the NiO layer.

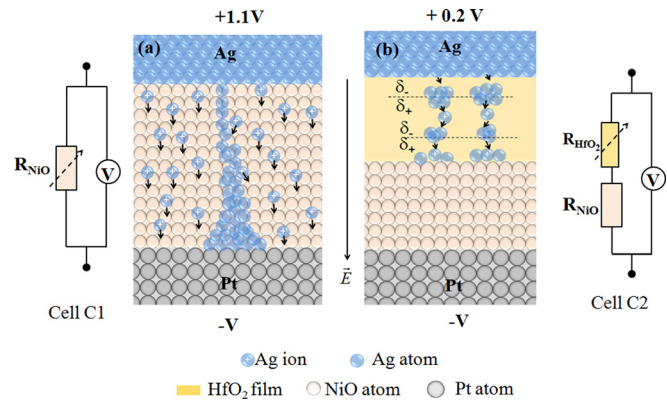


FIG. 9. Schematic of the simplified equivalent circuit model and the growth of Ag filaments in the (a) Cell C1 and (b) Cell C2 applied with a positive bias voltage on the Ag top electrode, respectively.

On the other hand, the HfO_2 layer exhibits new functionality. The O/Hf atom ratio in HfO_2 is larger than the O/Ni atom ratio in NiO. The larger oxygen concentration in the HfO_2 layer allows O^{2-} ions to accumulate near the Ag/ HfO_2 interface, generating a stronger internal electric field as per the Cabrera-Mott theory.²⁶ This internal field pulls Ag ions from the Ag electrode and injects them into the HfO_2 layer. It is suggested that Ag ions in the HfO_2 layer form clusters following the bipolar electrochemical mechanism.²⁷ Ag clusters dissolve from their original locations and nucleate at new positions closer to the Pt electrode in a process driven by the competing electrochemical processes occurring at the two polarized sides. Finally, these Ag clusters may constitute potential conductive channels across the HfO_2 layer via an oxygen ion-assisted “step-by-step” mechanism, as shown in Fig. 9(b). In this case, a positive bias as low as 0.2 V is sufficient to activate these channels by aligning these clusters. The HfO_2 layer replaces the NiO layer as the switching layer and NiO simply acts as serial resistor. A simplified equivalent circuit model is proposed in Fig. 9(b). If this model works, the ON-state resistance of Cell C2 should equal the effective resistance of the NiO layer. In fact, the ON-state current of Cell C2 is indeed on the same order of magnitude as the OFF-state current of Cell C1. When a negative bias is applied to the Ag electrode, the HfO_2 layer acts as a buffer and offers a larger OFF-resistance in series with the NiO layer. This is why the HfO_2 buffer reduces the switching voltage but enhances the ON/OFF ratio when the bias is low. However, if the bias is large enough (e.g., ± 1.1 V), dielectric breakdown in the HfO_2 layer allows Ag ion channels to penetrate into the NiO layer. The subsequent process is similar to the scenario in Fig. 9(a), which illustrates why the resistive switching characteristics of Cell C2 under high sweep voltages are similar to those in Cell C1. In our experiments with Cell C2 applied on a 0.2 V pulse, the fastest switching time is ~ 250 ns and the maximum ON-current is 0.78 mA; thus, 1.2×10^9 Ag ions are required to make Cell C2 switch to ON-state. This value is consistent with the result reported by Chu *et al.*²⁸ More details of the estimation process are given in the [supplementary material](#).

In conclusion, a high-quality NiO(001) film was grown epitaxially on a Pt (001) seed layer under tailored deposition conditions. Memory cells based on a Ag/NiO(001)/Pt stack

structure achieved a low switching voltage and large ON/OFF ratio. Upon inserting a HfO₂ buffer layer between the NiO (001) film and the Ag electrode, the ON/OFF ratio was improved by two orders of magnitude, and the switching voltage decreased to 0.2 V. This very low switching voltage enables possible applications in the next-generation of low energy consumption logic memory devices. Different filament growth mechanisms in the NiO and HfO₂ layers have been proposed to interpret this interesting phenomenon.

See [supplementary material](#) for details of film deposition and micro-structural characterization, electric measurement, and discussions on “oscillation” peaks and required Ag-ion quantity to make Cell C2 switch.

The authors acknowledge the financial support from the National Natural Science Foundation of China (Grant No. 11274257) and the Natural Science Foundation of Chongqing (Grant No. cstc2014jcyjA40029). J. Y. Dai is grateful to financial support of Hong Kong GRF Grant (Grant No. 15309416) and Internal Grant from the Hong Kong Polytechnic University (Grant Nos. 1_ZE25 and 1_BBAF).

- ¹D.-H. Kwon, K. M. Kim, J. H. Jang, J. M. Jeon, M. H. Lee, G. H. Kim, X.-S. Li, G.-S. Park, B. Lee, S. Han *et al.*, *Nat. Nanotechnol.* **5**, 148–153 (2010).
- ²J. Y. Seok, S. J. Song, J. H. Yoon, K. J. Yoon, T. H. Park, D. E. Kwon, H. Lim, G. H. Kim, D. S. Jeong, and C. S. Hwang, *Adv. Funct. Mater.* **24**, 5316–5339 (2014).
- ³H. Lim, I. Kim, J. S. Kim, C. S. Hwang, and D. S. Jeong, *Nanotechnology* **24**, 384005 (2013).
- ⁴J. F. Gibbons and W. E. Beadle, *Solid-State Electron.* **7**, 785–790 (1964).
- ⁵S. Seo, M. J. Lee, D. H. Seo, E. J. Jeoung, D.-S. Suh, Y. S. Joung, I. K. Yoo, I. R. Hwang, S. H. Kim, I. S. Byun *et al.*, *Appl. Phys. Lett.* **85**, 5655–5657 (2004).
- ⁶S. H. Chang, J. S. Lee, S. C. Chae, S. B. Lee, C. Liu, B. Kahng, D. W. Kim, and T. W. Noh, *Phys. Rev. Lett.* **102**, 026801 (2009).
- ⁷L. Goux, J. G. Lisoni, M. Jurczak, D. J. Wouters, L. Courtade, and C. Muller, *J. Appl. Phys.* **107**, 024512 (2010).
- ⁸M. Chowdhury, B. Long, R. Jha, and V. Devabhaktuni, *Solid-State Electron.* **68**, 1–3 (2012).

- ⁹S. Mitra, S. Chakraborty, and K. S. R. Menon, *Appl. Phys. A* **115**, 1173–1179 (2014).
- ¹⁰H. X. Zhu, J. Q. Huo, X. Y. Qiu, Y. Y. Zhang, R. X. Wang, Y. Chen, C.-M. Wong, H.-M. Yau, and J. Y. Dai, *Mater. Sci. Forum* **847**, 131–136 (2016).
- ¹¹K. Oka, T. Yanagida, K. Nagashima, H. Tanaka, and T. Kawai, *J. Am. Chem. Soc.* **131**, 3434–3435 (2009).
- ¹²J. Sullaphen, K. Bogle, X. Cheng, J. M. Gregg, and N. Valanoor, *Appl. Phys. Lett.* **100**, 203115 (2012).
- ¹³Y. D. Zhu and M. Li, *Adv. Condens. Matter Phys.* **2012**, 364376 (2012).
- ¹⁴S. R. Lee, H. M. Kim, J. H. Bak, Y. D. Park, K. Char, H. W. Park, D.-H. Kwon, M. Kim, D.-C. Kim, S. Seo *et al.*, *Jpn. J. Appl. Phys., Part 1* **49**, 031102 (2010).
- ¹⁵M. Kawai, K. Ito, and Y. Shimakawa, *Appl. Phys. Lett.* **95**, 012109 (2009).
- ¹⁶H. Inaba, *Jpn. J. Appl. Phys., Part 1* **35**, 4730–4735 (1996).
- ¹⁷I. N. Leontyev, A. A. Kulbakov, M. Allix, A. Rakhmatullin, A. B. Kuriganova, O. A. Maslova, and N. V. Smirnova, *Phys. Status Solidi B.* **254**, 1600695 (2017).
- ¹⁸X. Y. Qiu, R. X. Wang, G. Q. Li, T. Zhang, L. T. Li, M. L. Wei, X. S. Meng, H. Ji, Z. Zhang, C. H. Chan *et al.*, *Appl. Surf. Sci.* **406**, 212–217 (2017).
- ¹⁹K. P. Biju, X. J. Liu, E. M. Bourim, I. Kim, S. Jung, M. Siddik, J. Lee, and H. Hwang, *J. Phys. D: Appl. Phys.* **43**, 495104 (2010).
- ²⁰Y.-E. Syu, T. Ch. Chang, T.-M. Tsai, G.-W. Chang, K. Ch. Chang, J.-H. Lou, Y.-H. Tai, M.-J. Tsai, Y. L. Wang, and S. M. Sze, *IEEE Electron Device Lett.* **33**, 342–344 (2012).
- ²¹S. A. Mojarad, J. P. Goss, K. S. K. Kwa, Z. Zhou, R. A. S. Al-Hamadany, D. J. R. Appleby, N. K. Ponn, and A. O’Neill, *Appl. Phys. Lett.* **101**, 173507 (2012).
- ²²S. H. Jo, T. Kumar, S. Narayanan, and H. Nazarian, *IEEE Trans. Electron Devices* **62**, 3477–3481 (2015).
- ²³R. Midya, Z. Wang, J. Zhang, S. E. Savel’ev, C. Li, M. Rao, M. H. Jang, S. Joshi, H. Jiang, P. Lin *et al.*, *Adv. Mater.* **29**, 1604457 (2017).
- ²⁴Y. Yang, P. Gao, L. Li, X. Pan, S. Tappertzhofen, S. Choi, R. Waser, I. Valov, and W. D. Lu, *Nat. Commun.* **5**, 4232 (2014).
- ²⁵I. Valov, E. Linn, S. Tappertzhofen, S. Schmelzer, J. van den Hurk, F. Lentz, and R. Waser, *Nat. Commun.* **4**, 1771 (2013).
- ²⁶M. Saadi, P. Gonon, C. Vallee, C. Mannequin, H. Grampeix, E. Jalaguier, F. Jonni, and A. Bsiesy, *J. Appl. Phys.* **119**, 114501 (2016).
- ²⁷X. Tian, S. Yang, M. Zeng, L. Wang, J. Wei, Z. Xu, W. Wang, and X. Bai, *Adv. Mater.* **26**, 3649–3654 (2014).
- ²⁸T.-J. Chu, T.-C. Chang, T.-M. Tsai, H.-H. Wu, J.-H. Chen, K.-C. Chang, T.-F. Young, K.-H. Chen, Y.-E. Syu, G.-W. Chang *et al.*, *IEEE Electron Device Lett.* **34**, 502–504 (2013).